Research Square

Preprints are preliminary reports that have not undergone peer review.
They should not be considered conclusive, used to inform clinical practice,
or referenced by the media as validated information.

Doppler-Based GNSS Variometry for Velocity Estimation in High-Dynamic Sounding Rocket Missions

Carolina Ghini

carolina.ghini@gmail.com

Sapienza University

Augusto Mazzoni

Sapienza University

Research Article

Keywords: GNSS Variometry, Sounding Rockets, Doppler Observations, Velocity Estimation

Posted Date: August 12th, 2026

DOI: https://doi.org/10.21203/rs.3.rs-9493522/v1

License: This work is licensed under a Creative Commons Attribution 4.0 International License.
Read Full License

Additional Declarations: No competing interests reported.

Doppler-Based GNSS Variometry for Velocity Estimation in High-Dynamic Sounding Rocket Missions

Carolina Ghini[1*] and Augusto Mazzoni[1]

[1*] Department of Civil, Building and Environmental Engineering, Sapienza University, Via Eudossiana 18, Rome, 00184, Italy.

*Corresponding author(s). E-mail(s): carolina.ghini@gmail.com;
Contributing authors: augusto.mazzoni@uniroma1.it;

Abstract

This work investigates the application of GNSS variometry for onboard velocity estimation in sounding rocket flights, with particular focus on the use of Doppler observations under high-dynamic conditions. The study assesses, for the first time, the performance of a variometric algorithm originally developed for geodetic applications based on carrier-phase observations, here extended to Doppler observables in a high-dynamic aerospace scenario. The analysis is based on data acquired during two sounding rocket launch campaigns conducted in Roccaraso, Italy (May 2025), and Texas, USA (June 2025), using a lightweight Commercial Off-The-Shelf (COTS) payload composed of a Raspberry Pi single-board computer and dual u-blox ZED-F9P chipsets. Observations from GPS, Galileo, and BeiDou constellations on the L1 frequency were recorded simultaneously at different sampling rates, allowing a comparative evaluation of observation continuity and the corresponding variometric velocity solutions under both nominal and anomalous flight conditions. The results show that carrier-phase variometry, although associated with lower nominal uncertainty, is severely affected during the boost phase, where strong accelerations lead to degraded observation quality and incomplete reconstruction of the velocity peak. Doppler observations, by contrast, maintain continuity throughout all flight phases including the most demanding ones, and yield velocity estimates capable of reproducing the main features of the flight profile. Within the limitations of the available experimental dataset, the analysis suggests that Doppler-based variometry represents a robust and practically viable approach for GNSS velocity estimation in sounding rocket applications when carrier-phase continuity or integrity is reduced.

Keywords: GNSS Variometry, Sounding Rockets, Doppler Observations, Velocity Estimation

1 Introduction

In recent years, significant efforts have been devoted to the advancement of navigation solutions for high-dynamic aerospace platforms, including sounding rockets, launch vehicles, and suborbital missions. In these contexts, navigation performance depends on multiple processing layers, spanning from receiver-level signal tracking and raw observables generation to system-level state estimation and sensor fusion. At the receiver level, research has mainly focused on robust tracking architectures and dedicated high-dynamics algorithms capable of preserving signal lock and measurement continuity under severe acceleration, jerk, and attitude variations [4]. Flight evaluations of GPS receivers on sounding rockets have further highlighted the dependence of tracking performance on firmware design and hardware configuration [2], with more recent efforts directed toward miniaturized software-defined receivers for space applications [9]. At the navigation level, state estimation is commonly performed through tightly or loosely coupled GNSS/INS architectures based on Extended Kalman Filter (EKF) or Error-State Kalman Filter (ESKF) formulations, where GNSS observables, Doppler measurements, and inertial data from the IMU are fused to provide continuous estimates of position, velocity, and attitude throughout flight [5, 13, 14, 16].

Within this general navigation framework, the present work addresses an intermediate and complementary processing layer, located downstream of the receiver observables generation and upstream of the navigation filter. The objective is to investigate the reconstruction of high-accuracy velocity information directly from raw GNSS observables collected onboard during flight. The proposed approach is therefore conceived as an independent estimator complementary to the standard receiver navigation solution and potentially exploitable as an additional velocity input for subsequent GNSS/INS filtering architectures.

To this end, the variometric algorithm originally developed in [1] for precise geodetic applications — where it has been primarily employed with carrier-phase observations — is here investigated, for the first time, using Doppler observables in a spaceborne sounding rocket scenario. This extension is motivated by the robustness of Doppler observations under high-dynamic conditions, where carrier-phase continuity cannot be guaranteed. Although the present implementation is performed in post-processing, mainly due to the exploratory nature of this first application and the need for parameter tuning, the algorithm is inherently compatible with real-time onboard execution. The proposed algorithm can also be envisaged for future integration into the receiver firmware, with the estimated velocity provided as an additional real-time navigation output.

Among GNSS-based estimation techniques applicable to dynamic platforms, variometry – i.e., the estimation of velocity through time-differenced GNSS observables – represents a particularly attractive approach. Depending on the observable employed, three main formulations can be distinguished: code-based, carrier-phase-based, and

Doppler-based variometry. These differ significantly in terms of achievable accuracy, noise characteristics, and robustness under highly dynamic conditions. Code-based approaches are not considered in this work due to their limited accuracy. While carrier-phase solutions can provide very high precision, their applicability is strongly affected by cycle slips and loss of lock during critical flight phases. Doppler observations, on the other hand, offer a favorable trade-off between precision and robustness. All mission phases impose different levels of stress on the receiver tracking loops and may cause significant degradation in observation continuity, particularly for carrier-phase measurements [10].

In this work, two sounding rocket launch campaigns are analyzed, carried out at Roccaraso (Italy, May 2025) and in Texas (USA, June 2025), using a COTS GNSS payload. This choice is motivated by the relatively non-extreme dynamic conditions of the considered sounding rocket missions, representing a first assessment of the proposed variometric approach in a flight scenario. The objective is therefore not to rely on specialized high-dynamics hardware, but to evaluate whether meaningful and robust velocity information can be extracted directly from raw observables under realistic operational conditions.

The two campaigns differ in motor thrust, apogee altitude, and overall flight outcome. At each campaign, data were acquired simultaneously at two sampling frequencies in order to assess the impact of temporal resolution on observation continuity and velocity estimation performance.

Within this framework, the hardware architecture and the characteristics of the two flights are first described; observation continuity is then assessed across flight phases and sampling rates. The variometric framework is introduced alongside a static noise analysis that establishes the theoretical performance bounds of each observable; velocity estimates from both carrier-phase and Doppler observations are then compared against the NMEA reference over the full flight sequence and separately for each dynamic phase. Finally, the receiver clock drift is analyzed across all scenarios and related to the observed differences in variometric performance.

2 Set-up

The payload consists of a Raspberry Pi 4, two u-blox ZED-F9P GNSS receivers mounted on SparkFun boards and connected to two GNSS patch antennas, a battery, a voltage regulator and a heat sink. The hardware selection was primarily driven by the stringent size constraints imposed by the limited volume available in the rocket payload bay.

The two GNSS receivers were configured to acquire data simultaneously at 115200 bps while operating at different acquisition sampling frequencies. System outputs are provided in .ubx format, containing NMEA messages and RINEX files with raw code, phase and Doppler GNSS observations. It is worth noting that, whereas the variometric processing presented in this work relies exclusively on L1 observations from GPS, Galileo, and BeiDou, the ZED-F9P receiver computes its internal PVT solution by exploiting all available constellations (GPS, GLONASS, Galileo, BeiDou) on dual frequency (L1/L2), in conjunction with SBAS augmentation corrections. Consequently,

the NMEA output benefits from a broader and more comprehensive observation set than that employed in the variometric processing chain.

A summary of launches details is shown in Table 1.

Table 1 Launches Details.

Location	Date	Sampling Frequency 1	Sampling Frequency 2
Roccaraso	10/05/2025	1 Hz	5 Hz
Texas	12/06/2025	1 Hz	2 Hz

The Roccaraso launch reached a maximum altitude of approximately 1200 m, with a total flight duration of 128 s, and was successfully completed with nominal vehicle and payload performance.

The Texas launch, conducted with a higher-thrust motor, achieved an apogee of approximately 2600 m, with a total flight duration of 55 s.

The significantly shorter duration of the Texas flight is attributed to anomalies occurring during the mission. In particular, the airbrake system malfunctioned during the ascent phase, and the parachute failed to deploy during descent. Consequently, the vehicle entered a predominantly ballistic descent, maintaining high negative velocity toward ground.

Payload data are unavailable for the final seconds prior to ground impact, likely due either to an automatic shutdown triggered by elevated thermal conditions or to an abrupt system failure caused by the ground impact event.

3 Observations' Continuity

Observation continuity was assessed over the entire rocket flights to identify the most critical phases in terms of measurement density. In this context, continuity is defined as the availability, on an epoch-by-epoch basis, of a given observation from at least four satellites, all acquired at the same sampling frequency.

Doppler observations are continuously available throughout the flight. In contrast, carrier-phase observations exhibit significant discontinuities and are almost entirely absent during the initial high-acceleration phase of the flight.

For each launch campaign, a quantitative assessment of data completeness was performed for the GNSS phase observations.

Specifically, in Table 2, the following metrics are evaluated: the nominal expected epochs, defined as the theoretical number of observation epochs expected under continuous acquisition; the lost epochs, namely the epochs that do not satisfy the continuity condition introduced at the beginning of this section; and the percentage of lost epochs, computed as the ratio between the number of lost epochs and the nominal expected epochs, expressed as a percentage.

The results indicate that, from a quantitative perspective, increasing the acquisition frequency leads to a higher percentage of data loss. For this reason, the 1 Hz configuration was retained for both launches, consistently yielding 0% lost epochs.

Table 2 Expected and lost epochs for different sampling frequencies – Phase observations.

Launch site	Frequency	Expected Ep.	Lost Ep.	% Lost Epochs
Roccaraso	1 Hz	128	0	0%
	5 Hz	637	365	∼57%
Texas	1 Hz	55	0	0%
	2 Hz	110	37	∼34%

4 NMEA Solution

The rocket trajectory was obtained from NMEA messages acquired during both launch campaigns at the considered sampling frequencies.

The nominal flight profile can be described as a sequence of well-defined dynamic phases, in this case identifiable through the analysis of position and velocity trends obtained from the GNSS solution:

- Ascent I – Boost phase: A high-thrust regime characterized by strong positive acceleration and a rapid increase in velocity.
- Ascent II – Coast to apogee: Propulsive acceleration ceases and velocity progressively decreases.
- Apogee: The vertical velocity component approaches zero, marking the transition between ascent and descent.
- Descent I – Ballistic descent: The rocket accelerates toward the ground under gravity, exhibiting increasing negative velocity.
- Descent II – Parachute deployment: Aerodynamic drag significantly increases following parachute deployment, resulting in a marked reduction in descent velocity.
- Landing: The vehicle reaches ground level, and velocity converges to zero.

The Roccaraso launch exhibited all the nominal phases described above. In contrast, the Texas launch presented significant anomalies. As a result, the ascent phase was characterized by unstable behavior, including noticeable rocket oscillations. Moreover, during descent, instead of transitioning to a controlled deceleration phase, the rocket underwent continuous gravitational acceleration until ground impact, with no observable velocity attenuation associated with parachute deployment.

The NMEA velocity components in the ENU frame are derived as a finite differences computation of the positions between consecutive epochs.

5 GNSS Variometry

The variometric approach estimates receiver velocity by exploiting the time variation of GNSS observables between consecutive epochs.

Carrier-phase based variometry makes use of time-differenced observations

$$\Phi_r^s(t_{k+1}) - \Phi_r^s(t_k) = \frac{1}{\lambda}\big(\rho_r^s(t_{k+1}) - \rho_r^s(t_k)\big) + \frac{c}{\lambda}\big(\delta t_r(t_{k+1}) - \delta t_r(t_k)\big) + \Delta\eta_r^s \qquad (1)$$

while Doppler based variometry directly exploits the Doppler shift observed by the receiver's tracking loops:

$$D_r^s(t) = -\frac{1}{\lambda}\frac{d}{dt}\rho_r^s(t) - \frac{c}{\lambda}\Big(\dot{\delta t}_r(t) - \dot{\delta t}^{\,s}(t) + \nu_r^s(t)\Big) \tag{2}$$

The accuracy of variometric estimation depends on the type of observable employed, with carrier-phase variometry providing the highest precision at the millimeter-per-second level, while Doppler variometry offers a more robust solution with precision at the centimeter-per-second level [8].

5.1 Algorithm Implementation

For each satellite, the difference between observations at epochs t_k and t_{k+1} provides a measure of the displacement along the line of sight during the interval $\Delta t = t_{k+1} - t_k$; assembling this relationship across all visible satellites yields an overdetermined system solved via Weighted Least Squares (WLS).

The observation vector $\mathbf{y}$ contains, for each satellite s, the difference between the observables at the two epochs, expressed in metres. For carrier-phase variometry:

$$y_\Phi^s = \lambda\,\Phi_r^s(t_{k+1}) - \lambda\,\Phi_r^s(t_k) \quad [\mathrm{m}] \tag{3}$$

where λ is the carrier wavelength. Differencing over time cancels the integer ambiguity N_r^s, and the result represents the change in receiver-to-satellite range along the line of sight between the two epochs.

For Doppler-based variometry, the Doppler observable $D_r^s(t_k)$ (expressed in cycles per second) is converted into an equivalent range displacement:

$$y_D^s = -\lambda \cdot D_r^s(t_{k+1}) \cdot \Delta t \quad [\mathrm{m}] \tag{4}$$

representing the instantaneous range displacement along the line of sight reconstructed from the Doppler shift at epoch t_{k+1}.

After applying corrections for satellite clock drift variation, tropospheric delay variation, and ionospheric delay variation, the linearized system is assembled as:

$$\mathbf{y} = \mathbf{A}\,\mathbf{x} + \mathbf{v}, \qquad \mathbf{x} = \begin{bmatrix}\Delta X & \Delta Y & \Delta Z & c\,\Delta\delta t_r\end{bmatrix}^\top \quad [\mathrm{m}] \tag{5}$$

where $\mathbf{A}$ is the design matrix of line-of-sight unit vectors at epoch t_{k+1}; $\mathbf{x}$ contains the three receiver displacement components in ECEF coordinates and the receiver clock offset variation $c\,\Delta\delta t_r$, all expressed in metres; and $\mathbf{v}$ is the observation noise vector.

The WLS solution is obtained as:

$$\hat{\mathbf{x}} = \left(\mathbf{A}^\top\mathbf{W}\mathbf{A}\right)^{-1}\mathbf{A}^\top\mathbf{W}\,\mathbf{y} \tag{6}$$

where $\mathbf{W} = \mathrm{diag}(\cos^2 e_i)$ is the diagonal weight matrix, with e_i denoting the elevation angle of the i-th satellite. The estimated displacement vector $(\Delta X, \Delta Y, \Delta Z)$ is then

divided by Δt to obtain the receiver velocity in ECEF:

$$\dot{\mathbf{p}} = \frac{\hat{\mathbf{x}}_{1:3}}{\Delta t} \quad [\text{m/s}] \tag{7}$$

A minimum elevation cutoff of 5° is applied to exclude satellites below the horizon mask. Tropospheric delay variations are modelled using the Saastamoinen model [12]; ionospheric delay variations are accounted for using the Klobuchar model, applied in single-frequency mode on the L1 signal [15]. Satellite clock corrections are derived from the broadcast navigation messages, including group delay differentials (TGD).

An outlier rejection step is applied after the initial WLS solution: observations whose post-fit residuals exceed a predefined threshold σ_{thr} are flagged and excluded, and the solution is recomputed on the remaining observations.

The estimated velocity components $(\dot{X}, \dot{Y}, \dot{Z})$ in ECEF are subsequently rotated into the local geodetic frame to obtain the East, North, and Up velocity components reported in the results. The receiver clock drift rate $\dot{\delta t}_r$ is obtained analogously by dividing $c\,\Delta\delta t_r$ by Δt, and is analyzed separately in Section 7.

The algorithm is implemented in post-processing mode; however, the epoch-by-epoch structure of this WLS estimator makes it inherently compatible with real-time onboard execution, as no future observations are required at any processing step.

5.2 Static Analysis – Noise

A statistical analysis is conducted by comparing the variometric solutions to the static configuration (i.e. zero velocity for all the components) to find the noise level for all the three raw observations and to assess the reachable accuracy of the entire system.

The performances for 1 hour acquisition are reported in terms of RMSE (Root Mean Square Error). The results are related to each observation for every sampling frequency.

Data acquisition was carried out on the rooftop of the university building under open-sky conditions. Given the optimal acquisition conditions of the system, the number of discarded epochs was considered negligible and is therefore not reported.

Table 3 Velocity accuracies along East (E), North (N), and Up (UP) directions for different GNSS variometry types – 1 hour acquisition.

Observation	E [m/s]	N [m/s]	UP [m/s]
Pseudorange	0.089	0.129	0.327
Phase	0.002	0.002	0.003
Doppler	0.013	0.015	0.038

Here, E, N, and Up represent the 3-D velocity components in local Cartesian coordinates projected onto the local geodetic frame [7]. The results clearly indicate that code observations provide the lowest accuracy among the considered observables, whereas carrier-phase measurements yield the highest accuracy. Doppler observations

exhibit intermediate performance. These findings align with the previously introduced theory and confirm the results reported in the variometry literature [3].

5.3 Velocity Estimation Results

For the Roccaraso dataset, both RINEX files provided valid solutions using both carrier-phase and Doppler observations.

By contrast, in the Texas dataset, carrier-phase measurements were available only for the descent and exclusively from GLONASS and SBAS satellites, which were not included in the computations; as a result, no usable carrier-phase solution could be obtained. Doppler observations, however, remained available throughout the flight and allowed a complete solution.

The results of the variometric estimation are illustrated in the following figures and Table 4.

Table 4 Velocity solution precision statistics (mm/s)

Launch	Case	Min (mm/s)	Max (mm/s)	Mean (mm/s)
Roccaraso	1 Hz Dopp	1	590	84
Roccaraso	1 Hz Phase	<1	279	15
Roccaraso	5 Hz Dopp	2	595	84
Roccaraso	5 Hz Phase	<1	279	14
Texas	1 Hz Dopp	6	1609	191
Texas	2 Hz Dopp	3	399	59

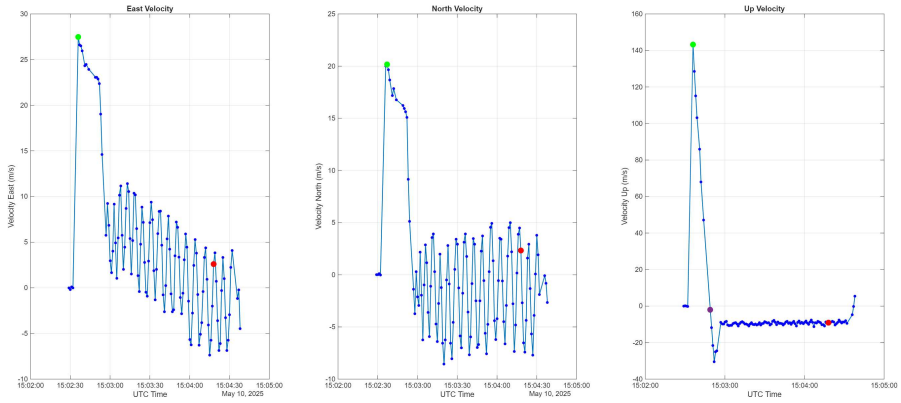


Fig. 1 Doppler Variometry Roccaraso – 1 Hz.

Regarding the Roccaraso launch it is evident that, for both acquisition frequencies, the carrier-phase-based solution exhibits significantly lower uncertainty, but it includes only a few valid points and is unable to reproduce the achieved velocity peak, whereas the Doppler solution successfully captures it at both sampling rates.

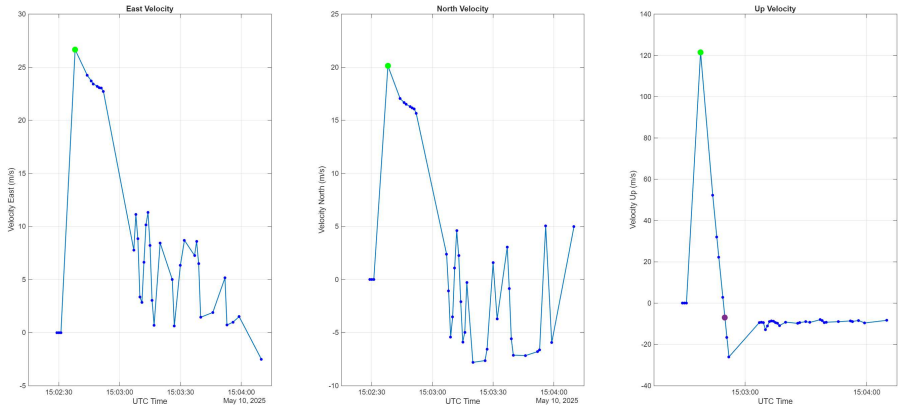


Fig. 2 Phase Variometry Roccaraso – 1 Hz.

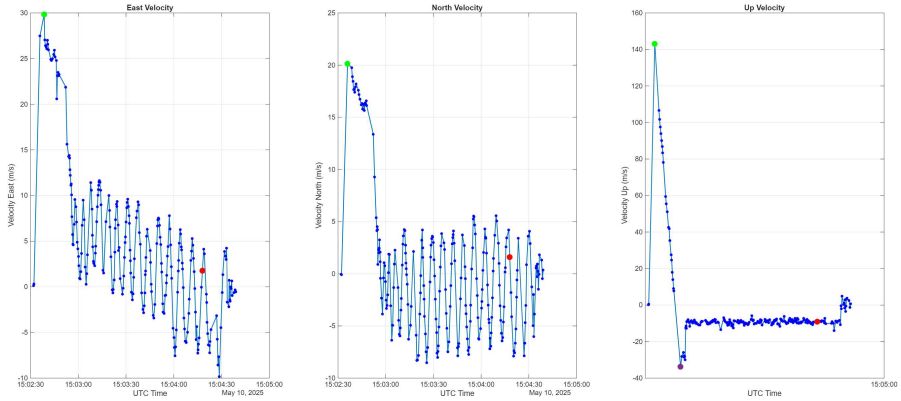


Fig. 3 Doppler Variometry Roccaraso – 5 Hz.

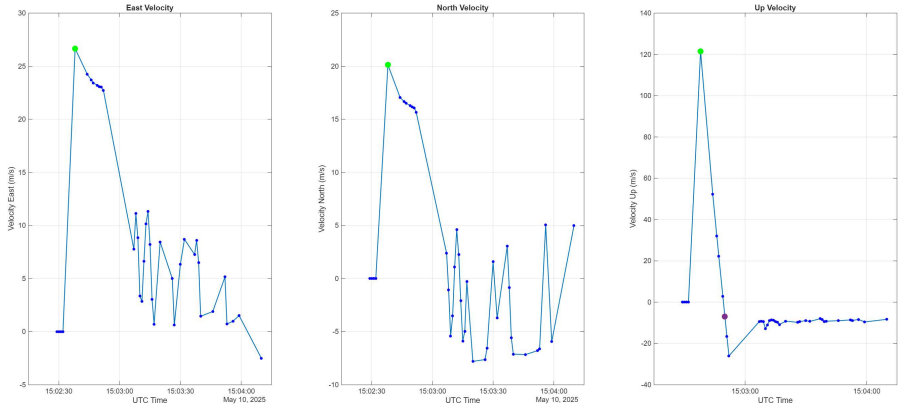


Fig. 4 Phase Variometry Roccaraso – 5 Hz.

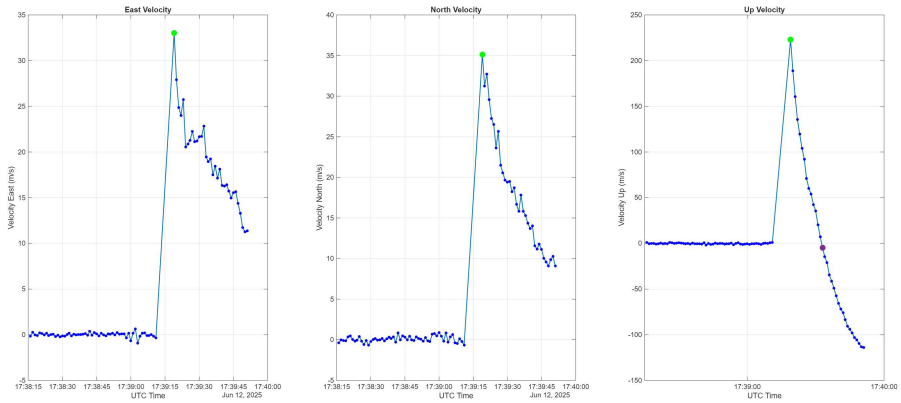


Fig. 5 Doppler Variometry Texas – 1 Hz.

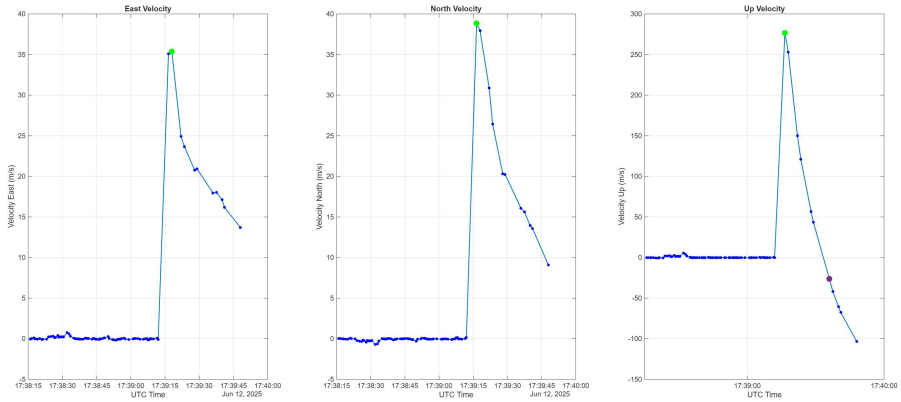


Fig. 6 Doppler Variometry Texas – 2 Hz.

For the Texas launch, both datasets fail to fully capture the actual velocity peak. The 2 Hz solution approximates it within a few meters, while the 1 Hz solution falls short by approximately 80 m/s, resulting in an inaccurate representation of the high-acceleration segment.

6 Velocities Comparison

A comparison between variometric solutions and NMEA-derived velocity was performed to assess the relative performance of the proposed estimation approaches, as no independent trajectory reference was available for either campaign.

The NMEA-derived velocity is acknowledged as an imperfect reference, as it originates from the same receiver hardware used to collect the raw observables; nevertheless, it is considered an adequate benchmark for the present analysis because it ensures an adequate solution for all mission phases including acceleration boost and is derived from a position-domain filter structurally independent from the variometric processing chain. Furthermore, the asymmetry between the two solutions should

be emphasized: the NMEA reference exploits dual-frequency observations from four constellations and SBAS augmentation, while the variometric solution relies exclusively on single-frequency L1 Doppler observations from three constellations. The fact that the proposed approach achieves competitive velocity estimates under these more constrained conditions supports the robustness of Doppler-based variometry as a standalone estimation technique.

NMEA and variometry velocity solutions provide a different number of valid epochs, even when acquired at the same sampling rate. For this reason, all statistics are computed only over the epochs for which a variometric estimation is available and coincides with an epoch of NMEA-derived velocity. The number of such coincident epochs is reported in Table 5 and the results in terms of RMSE are reported in Table 6.

Table 5 Number of epochs for each data set and common epochs.

Case	Expected Epochs	NMEA	Variometry	Common
1 Hz Rocc. Doppler	128	128	113	103
1 Hz Rocc. Phase	128	128	34	34
5 Hz Rocc. Doppler	637	381	233	170
5 Hz Rocc. Phase	637	381	35	19
1 Hz Texas Doppler	55	39	49	34
2 Hz Texas Doppler	110	73	29	11

Concerning temporal density, the 5 Hz Doppler-based solution provides the highest number of solution epochs for the Roccaraso launch. For the Texas launch, the 1 Hz solution yields approximately three times more solution points than the 2 Hz case. The Roccaraso 1 Hz case is the only scenario in which the NMEA solution provides the full set of expected epochs. At 5 Hz, for the same launch, the number of available NMEA epochs is significantly reduced compared to the nominal condition. For the Texas 1 Hz case, the number of NMEA epochs is even lower than the number of epochs estimated through variometric processing.

It should be emphasized that the number of coincident epochs varies considerably across configurations and flight phases, and this has a direct bearing on the interpretation of the RMSE values reported below. In particular, the carrier-phase solutions contribute very few valid epochs, concentrated almost exclusively in the coast and descent phases; the boost phase, where the largest velocity gradients occur, is therefore largely absent from the corresponding accuracy computation.

Table 6 refers to the entire launch sequence, from the boost phase to landing. Although it provides a general overview of the deviations from the NMEA reference, it does not fully reflect the evolution of the solution throughout the different phases of the flight.

In Table 7 and Table 8, both launches have been analyzed by computing the statistics separately for three distinct phases: Ascent I, Ascent II and Descent.

Partitioning the solution epochs according to the flight phases provides a clearer picture of the differences in observation density between Doppler and carrier-phase solutions across the flight sequence. The RMSE values are reported for completeness

Table 6 RMSE along East (E), North (N), and Up (U) directions for different observation cases and solution epochs.

Case	RMSE E [m/s]	RMSE N [m/s]	RMSE U [m/s]
1 Hz Rocc. Doppler	1.676	1.747	1.925
1 Hz Rocc. Phase	0.5507	0.421	0.782
5 Hz Rocc. Doppler	1.013	0.919	1.701
5 Hz Rocc. Phase	0.941	0.932	1.658
1 Hz Texas Doppler	1.277	1.427	7.861
2 Hz Texas Doppler	0.916	0.818	4.515

and to give an indication of the order of magnitude of the deviations, but should be interpreted in light of the epoch counts reported alongside them.

In particular, the small number of coincident epochs during Ascent I reflects the brevity of the boost phase in both campaigns – a physical property of the missions considered – combined with the rapid degradation of carrier-phase observations under strong acceleration. This is not a limitation of the proposed approach, but an inherent constraint imposed by the nature and the duration of the event itself. Within these constraints, the phase-by-phase breakdown is nonetheless useful to show that Doppler observations consistently yield a higher number of valid epochs than carrier-phase across all flight phases, including the most dynamic ones.

Table 7 RMSE along E, N, and U directions and solution epochs for Doppler and Phase observations during Ascent I, Ascent II, and Descent.

Obs	Ascent I	Ascent II	Descent
Doppler (1 Hz)	Epochs N. = 3	Epochs N. = 6	Epochs N. = 104
	RMSE E = 0.312 m/s	RMSE E = 0.320 m/s	RMSE E = 1.838 m/s
	RMSE N = 0.773 m/s	RMSE N = 0.516 m/s	RMSE N = 1.865 m/s
	RMSE U = 7.864 m/s	RMSE U = 7.742 m/s	RMSE U = 1.271 m/s
Phase (1 Hz)	Epochs N. = 3	Epochs N. = 5	Epochs N. = 26
	RMSE E = 0.219 m/s	RMSE E = 0.159 m/s	RMSE E = 0.614 m/s
	RMSE N = 0.036 m/s	RMSE N = 0.360 m/s	RMSE N = 0.452 m/s
	RMSE U = 0.126 m/s	RMSE U = 1.710 m/s	RMSE U = 0.524 m/s
Doppler (5 Hz)	Epochs N. = 2	Epochs N. = 16	Epochs N. = 159
	RMSE E = 1.166 m/s	RMSE E = 0.477 m/s	RMSE E = 0.958 m/s
	RMSE N = 0.269 m/s	RMSE N = 0.353 m/s	RMSE N = 0.960 m/s
	RMSE U = 1.734 m/s	RMSE U = 2.250 m/s	RMSE U = 1.617 m/s
Phase (5 Hz)	Epochs N. = 1 (static)	Epochs N. = 4	Epochs N. = 14
	RMSE E = 0.008 m/s	RMSE E = 0.077 m/s	RMSE E = 1.175 m/s
	RMSE N = 0.063 m/s	RMSE N = 0.204 m/s	RMSE N = 1.026 m/s
	RMSE U = 0.306 m/s	RMSE U = 2.234 m/s	RMSE U = 1.195 m/s

For the Roccaraso launch, as shown in Figure 2 and Figure 4, the velocity peak is absent from the phase-based solution, which reaches a maximum of approximately 120 m/s instead of 150 m/s. The lower RMSE of the phase-based solution therefore partly reflects the exclusion of the most dynamically demanding epochs, rather than a genuine advantage over the full flight sequence.

The Doppler-based solution, by contrast, maintains sufficient observation quality throughout the boost phase, successfully reproducing the velocity peak at both sampling rates. Among the Doppler configurations, the 5 Hz solution offers the best overall compromise between temporal density and coverage of the flight dynamics, effectively reproducing the velocity peak and the full descent profile, with deviations from the NMEA reference of 1.6–2.4 m/s along the UP axis and 0.3–1.0 m/s along the E and N axes.

Table 8 RMSE along E, N, and U directions and solution epochs for 1 Hz and 2 Hz observations during Ascent I, Ascent II, and Descent.

Obs	Ascent I	Ascent II	Descent
1 Hz	Epochs N. = 2 (static)	Epochs N. = 14	Epochs N. = 18
	RMSE E = 0.225 m/s	RMSE E = 1.878 m/s	RMSE E = 1.075 m/s
	RMSE N = 0.460 m/s	RMSE N = 2.054 m/s	RMSE N = 0.742 m/s
	RMSE U = 0.753 m/s	RMSE U = 11.508 m/s	RMSE U = 3.924 m/s
2 Hz	Epochs N. = 2 (static)	Epochs N. = 5	Epochs N. = 4
	RMSE E = 0.071 m/s	RMSE E = 1.303 m/s	RMSE E = 0.430 m/s
	RMSE N = 0.081 m/s	RMSE N = 1.138 m/s	RMSE N = 0.468 m/s
	RMSE U = 0.115 m/s	RMSE U = 5.612 m/s	RMSE U = 4.085 m/s

For the Texas campaign, regarding the Doppler-only comparison between sampling rates, the 2 Hz solution achieves lower deviations from the NMEA reference compared to the 1 Hz solution across all components, and better captures the high-dynamics phase of the trajectory. This result should however be read in light of the very different number of coincident epochs available for the two configurations (11 vs. 34), which limits the statistical robustness of the comparison.

The UP component, which experienced stronger acceleration during this launch compared to the Roccaraso campaign, shows deviations of approximately 5 m/s from the NMEA reference; the E and N components range from 0.5 to 1.3 m/s. These results are considered acceptable given the complexity of the flight scenario with high thrust, uncontrolled oscillatory motion, and anomalous descent.

Taken together, the two campaigns provide complementary evidence of the same underlying behavior: carrier-phase variometry is more susceptible to degradation under high-dynamics conditions, whether through observation rejection or outright loss of lock, while Doppler variometry maintains robustness in both scenarios. The consistency of this finding across two campaigns with substantially different characteristics suggests that the observed behavior is not specific to a particular mission profile, but may reflect a more general property of these observables under high-acceleration conditions. Nonetheless, the limited number of experimental campaigns considered here does not allow for broad generalization, and further validation on a larger dataset would be required to confirm this hypothesis.

7 Clock Drift

Clock drift represents the temporal deviation of the receiver's internal clock with respect to GNSS system time. Expressed in s/s, this parameter provides a measure of clock stability and is influenced by environmental conditions (e.g., vibrations and temperature variations) as well as by system configuration, including sampling frequency and platform dynamics. It is well documented that GNSS receiver clocks onboard dynamic platforms may exhibit oscillations and transient behaviors associated with flight conditions and filter convergence [11].

The analysis of clock drift across the two launch campaigns reveals behaviors that are consistent with the differences in flight dynamics and hardware configuration observed in the previous sections.

For the Roccaraso launch, the clock drift exhibits a relatively stable mean at both sampling frequencies (2.41×10^{-7} s/s at 1 Hz and 2.11×10^{-7} s/s at 5 Hz), while the standard deviation remains essentially unchanged ($\sim 0.27 \times 10^{-7}$ s/s). This consistency suggests that the oscillatory behavior of the clock is largely insensitive to sampling rate in the moderate-dynamics environment of the Roccaraso flight.

The Texas launch presents a fundamentally different picture. At 1 Hz, the clock drift is the most stable of all scenarios (mean 2.35×10^{-7} s/s, standard deviation 0.12×10^{-7} s/s), likely reflecting the shorter data record and the absence of a post-parachute low-dynamics phase due to the deployment failure. However, when the sampling frequency is increased to 2 Hz, the mean drift rises substantially to 3.60×10^{-7} s/s, with a corresponding increase in standard deviation to 0.25×10^{-7} s/s. This behavior is consistent with the more severe aerodynamic and inertial environment of the Texas trajectory – in particular, the uncontrolled oscillations during ascent and the ballistic descent phase. Higher sampling rates are more sensitive to rapid clock variations induced by vibration and thermal transients, and the anomalous dynamics of the Texas flight amplified these effects beyond what was observed at Roccaraso. Overall, the clock drift results are coherent with the variometric findings: the increased variability and higher mean drift observed in the Texas 2 Hz dataset are consistent with the reduced solution continuity and the greater measurement uncertainty reported for that configuration.

8 Conclusions

This study investigated the performance of GNSS-based velocity estimation for sounding rockets using a COTS payload system across two launch campaigns conducted at Roccaraso (Italy, May 2025) and Texas (USA, June 2025). The analysis encompassed three complementary aspects: observation continuity, variometric velocity solution, and estimation accuracy, evaluated under both nominal and anomalous flight conditions. It should be noted that, due to the operational constraints of the campaigns, no independent trajectory reference was available; the NMEA-derived solution from the same receiver hardware was used as a benchmark. Although this constitutes a limitation, the NMEA solution is considered adequate for comparative purposes, as it relies on a position-domain filter structurally distinct from the variometric processing chain, and exhibits stable fix availability throughout both flights.

With regard to observation continuity, the results consistently demonstrate that 1 Hz acquisition yields complete carrier-phase coverage (0% lost epochs) in both campaigns, whereas higher sampling rates introduce significant epoch losses. This degradation is concentrated in the high-acceleration phases of the flight, where carrier-phase tracking is most susceptible to signal stress. Doppler observations, by contrast, maintained full continuity at all tested frequencies, confirming its robustness under highly dynamic conditions.

Concerning velocity estimation, the two campaigns are discussed separately, as they present substantially different flight profiles and data availability.

For the Roccaraso campaign, both carrier-phase and Doppler variometric solutions were obtained at 1 Hz and 5 Hz. Carrier-phase observations yield lower solution uncertainty relative to the NMEA reference, consistent with their millimeter-per-second noise floor as characterized in the static analysis; however, they provide only a sparse set of valid epochs and systematically fail to resolve the velocity peak during the boost phase, reaching a maximum reconstructed velocity of approximately 120 m/s against the 150 m/s estimated by the Doppler solution. Doppler-based variometry, by contrast, maintains full observation continuity throughout all flight phases and successfully reproduces the velocity peak at both sampling rates. The 5 Hz Doppler solution offers the best compromise between temporal density and accuracy relative to the NMEA reference, providing the highest number of coincident solution epochs across all flight phases. These results suggest that, when carrier-phase continuity cannot be guaranteed, Doppler variometry represents a more robust alternative for capturing short-duration dynamic events, at the cost of higher solution uncertainty.

For the Texas campaign, no usable carrier-phase solution could be obtained owing to the unavailability of the required constellations throughout the flight; the analysis is therefore restricted to Doppler observations at 1 Hz and 2 Hz. The 2 Hz solution achieves markedly lower deviations from the NMEA reference across all three components compared to the 1 Hz solution, and approximates the velocity peak within a few meters per second, whereas the 1 Hz solution underestimates it by approximately 80 m/s.

Clock drift analysis provided results consistent with the variometric findings. The Roccaraso launch exhibited stable and consistent clock behavior across both sampling frequencies, reflecting the nominally controlled flight profile. The Texas campaign showed a substantial increase in mean drift and variability when transitioning from 1 Hz to 2 Hz, consistent with the more severe dynamic environment and the amplified sensitivity of higher-frequency sampling to rapid oscillator perturbations induced by vibration and thermal transients.

Taken together, these results support the use of Doppler-based GNSS variometry as a candidate approach for velocity estimation in sounding rocket applications, particularly in scenarios where carrier-phase continuity cannot be guaranteed. Future investigations should extend the proposed approach to missions equipped with independent reference systems – such as inertial navigation units or ground-based tracking – to enable an absolute assessment of the achievable accuracy, and should consider extending the variometric processing to multi-constellation and dual-frequency observations.

Acknowledgements. We gratefully acknowledge the Sapienza Aerospace Student Association, and especially the Sapienza Rocket Team, for their contributions to the design and integration of the rocket system.

References

[1] Branzanti M, Colosimo G, Mazzoni A. Variometric approach for real-time GNSS navigation: First demonstration of Kin-VADASE capabilities. *Adv Space Res.* 2017;59(11):2750–2763.

[2] Bull B, Diehl J, Montenbruck O, Markgraf M. Flight Performance Evaluation of Three GPS Receivers for Sounding Rocket Tracking. In: *Proc 2002 National Technical Meeting of the Institute of Navigation.* San Diego, CA; 2002. pp. 614–621.

[3] Colosimo G, Crespi M, Mazzoni A. Real-time GPS seismology with a stand-alone receiver: A preliminary feasibility demonstration. *J Geophys Res Solid Earth.* 2011;116:B11302.

[4] Conde N, Gupta H, Cortés I, Overbeck M, Ackermann J, Welham M, Rügamer A. Comprehensive Evaluation of Simulated Launcher Scenarios Using Space a GNSS Receiver. In: *Proc 38th Int Tech Meeting of the Satellite Division of the Institute of Navigation (ION GNSS+).* 2025. pp. 437–445.

[5] Groves PD. Principles of GNSS, Inertial, and Multisensor Integrated Navigation Systems. 2nd ed. London: Artech House; 2013.

[6] Guzzi S, Longo R, Bernardi F, Fantinato S, Pozzobon O, Miller JJ, et al. GARSPACE GNSS Receiver Experimentation Results During SL-15 Sounding Rocket Launch. In: *Proc 38th Int Tech Meeting of the Satellite Division of the Institute of Navigation (ION GNSS+).* 2025. pp. 1867–1880.

[7] Jekeli C, Montenbruck O. Time and Reference Systems. In: Teunissen PJG, Montenbruck O, editors. *Springer Handbook of Global Navigation Satellite Systems.* Cham: Springer International Publishing; 2017. pp. 25–58.

[8] Ji L, Sun R, Cheng Q, Wang J. Evaluation of the performance of GNSS-based velocity estimation algorithms. *Satell Navig.* 2022;3:18.

[9] Lightsey EG, Humphreys TE, Bhatti JA, Joplin AJ, O'Hanlon BW, Powell SP. Demonstration of a Space Capable Miniature Dual Frequency GNSS Receiver. *J Inst Navig.* 2014;61:53–64.

[10] MacGougan G, Lachapelle G, Nayak R, Wang A. Overview of GNSS Signal Degradation Phenomena. In: *Proceedings of the Kinematic International Symposium (KIS01).* Banff, Canada; 2001.

[11] Misra P, Enge P. Global Positioning System: Signals, Measurements, and Performance. Revised 2nd ed. Lincoln, MA: Ganga-Jamuna Press; 2011.

[12] Saastamoinen J. Atmospheric Correction for the Troposphere and Stratosphere in Radio Ranging Satellites. In: Henriksen SW, Mancini A, Chovitz BH, editors. *The Use of Artificial Satellites for Geodesy*. Vol. 15; 1972. pp. 247–251.

[13] Solano-López P, de Celis R, Fuentes M, Cadarso L, Barea A. Strategies for high performance GNSS/IMU Guidance, Navigation and Control of Rocketry. In: *Proc 8th Eur Conf Aeronautics and Aerospace Sciences (EUCASS)*. 2019.

[14] Vandersteen J, Bennani S, Roux C. Robust Rocket Navigation with Sensor Uncertainties: Vega Launcher Application. *J Spacecr Rockets*. 2018;55(1):1–14.

[15] Yuan Y, Li X, Liu L, Zhang J. Refining the Klobuchar ionospheric coefficients based on GPS observations. *IEEE Trans Aerosp Electron Syst*. 2008;44(4):1498–1510.

[16] Zhou Z, Li B. Optimal Doppler-aided smoothing strategy for GNSS navigation. *GPS Solut*. 2017;21:197–210.